Supporting information

Layered Hexagonal Oxycarbides, $M_{n+1}AO_2X_n$ (M=Sc, Y, La, Cr and Mo, A=Ca, X=C): Unexpected Photovoltaic Ceramics

Zhenyu Wang,[†] Xin Chen,[*,†] and Chunming Niu[*,†]

[†]*Center of Nanomaterials for Renewable Energy (CNRE), State Key Lab of Electrical Insulation and Power Equipment, School of Electrical Engineering, Xi'an Jiaotong University, 99 Yanxiang Road, Xi'an 710054, China. *E-mail: xin.chen.nj@xjtu.edu.cn; *E-mail: cniu@mail.xjtu.edu.cn.*

Section S1. Formation Energy

The formation energy of M_2CaO_2C is estimated based on the following chemical reaction:

$$\frac{3}{2y}M_xO_y + (2 - \frac{3x}{2y})M + \frac{1}{2}CaO + \frac{1}{2}CaC_2 = M_2CaO_2C$$

And

$$2M + CaO + CO = M_2CaO_2C,$$

which is calculated by:

$$\Delta G_f = E(M_2CaO_2C) - \frac{3}{2y}E(M_xO_y) - (2 - \frac{3x}{2y})E(M) - \frac{1}{2}E(CaO) - \frac{1}{2}E(CaC_2) \quad (S1)$$

and

$$\Delta G_f = E(M_2CaO_2C) - 2E(M) - E(CaO) - E(CO), \quad (S2)$$

where $E(M_2CaO_2C)$, $E(M_xO_y)$, $E(CaO)$, $E(CaC_2)$, $E(M)$ and $E(CO)$ indicate the total energy of M_2CaO_2C, M oxide, CaO, CaC_2 per formula, metal M in the ground state per atom and CO gas per molecule, respectively.

Section S2. Effective Masses

The effective masses of the MAOX semiconductors are calculated by the parabolic model:

$$E = \frac{\hbar^2 k^2}{2m^*}, \quad (S3)$$

where k is the wave vector, and m^* is the effective mass.

Due to the layered structure of MAOX phase, we take two directions for the effective masses: the parallel one corresponds to the a_1-a_2 plane ($m^{||}$) and the perpendicular one to the c axis ($m^{\perp}$). Using the band dispersion in Figure 4, the parallel and perpendicular effective masses are presented in Table S2. The parallel electron/hole effective masses are the averages of the two k-point directions and labeled with bold numbers in Table S2. In particular, the hole effective masses of Cr_2CaO_2C and Mo_2CaO_2C are not considered because their valence band maximum does not occur at high-symmetry k-points.

Section S3. Photovoltaic Efficiency

The SQ limit model has the conversion efficiency maximum around the optical bandgap of 1.34 eV based on the detailed balance and optical bandgap.[1, 2] The better estimation for the conversion efficiency is the spectroscopic limited maximum efficiency (SLME),[3] which takes both non-radiative effects and film absorption into account beyond the SQ limit. To eliminate the broadening of absorption edge caused by Gaussian smearing, the dielectric functions are calculated using HSE06 hybrid functional with tetrahedron method.[4]

In the SLME model, a photovoltaic cell is treated as an ideal diode illuminated under the incident photon flux I_{sun}.[3] In this case, the total current can be calculated as follows,

$$J = J_{sc} - J_0(1 - e^{\frac{eV}{kT}}), \quad (S4)$$

J_{sc} is the the short-circuit current density given by,

$$J_{sc} = e\int_0^\infty a(E)I_{sun}(E)dE = e\int_0^\infty (1 - exp(-2\alpha(E)L))I_{sun}(E)dE, \quad (S5)$$

where α and L are the absorption coefficient and thickness,

and J_0 is reverse saturation current given by,

$$J_0 = f_r^{-1}J_0^r = f_r^{-1}e\int_0^\infty a(E)I_{bb}(E,T)dE = f_r^{-1}e\int_0^\infty (1 - exp(-2\alpha(E)L))I_{bb}(E,T)dE, \quad (S6)$$

$$f_r = e^{-\frac{E_g^{dir} - E_g^{ind}}{kT}}, \quad (S7)$$

where f_r, I_{bb}, E_g^{ind} and E_g^{dir} are the fraction of the radiative recombination current, the black-body radiation flux, the indirect bandgap and direct bandgap, respectively.

The maximum energy conversion efficiency, η, is given by,

$$\eta = \frac{[JV]_{max}}{P_{in}}, \quad (S8)$$

where $[JV]_{max}$ and P_{in} are the maximum electrical output power density and the total incident solar power density, respectively.

Section S4. Calculation of Elastic Constants

We have estimated the shear modulus K and bulk modulus G of polycrystalline aggregates from individual elastic (c_{ij}) and compliance constants (s_{ij}) with the Voigt and Reuss approximations.[5, 6] The shear (K) and bulk moduli (G) labeled with the subscripts V and R corresponding to the Voigt and Reuss approximations are defined as:

$$K_V = \frac{1}{9}(2c_{11} + 2c_{12} + 4c_{13} + c_{33}), \quad (S9)$$

$$K_R = \frac{1}{2s_{11} + 2s_{12} + 4s_{13} + s_{33})}, \quad (S10)$$

$$G_V = \frac{1}{15}(2c_{11} + c_{33} - c_{12} - 2c_{13}) + \frac{1}{5}(2c_{44} + c_{66}), \quad (S11)$$

and

$$G_R = \frac{1}{(2s_{11} + s_{33}) + 2(s_{12} + 2s_{13})}. \quad (S12)$$

The shear (K) and bulk moduli (G) presented in Table S3 are based on the Voigt-Reuss-Hill approximation,[7] the average according to the Voigt and Reuss approximations，

$$K = \frac{1}{2}(K_V + K_R) \quad (S13)$$

and

$$G = \frac{1}{2}(G_V + G_R). \quad (S14)$$

The Young's modulus (E) and Poisson's ratio (v) are estimated according to the following formula:

$$E = \frac{9KG}{3K + G} \quad (S15)$$

and

$$v = \frac{3K - 2G}{2(3K + G)}. \quad (S16)$$

Table S1. The reported bandgaps (eV) of 2D MXenes (M= Sc, Y, La, Ti, Zr, Hf and Mo) with different functional groups (O, –F, –OH)

MXene	Functional groups		
	O	–F	–OH
Sc_2C	1.8[a], 1.86[b]	1.03[a], 1.03[b], 1.0[d]	0.45[a], 0.56[b], 0.71[d]
Y_2C	1.32[b]	1.14[b]	0.47[b]
La_2C	0.6[b]	1.02[b]	0.64[b]
Ti_2C	0.24[a], 0.32[b], 0.33[c], 0.17[d]	-	-
Zr_2C	0.88[a], 0.97[b], 0.95[c], 0.66[d]	-	-
Hf_2C	1.0[a], 1.03[b], 1.00[c],	-	-

		0.8[d]		
Mo_2C	-	0.05[d]	0.1[d]	

[a]Ref.8, [b]Ref.9, [c]Ref.10, [d]Ref.11.

Table S2. Formation energy (ΔG_f) of MAOX phase and the competing phase in the estimation, where the space groups of M oxides are in the parentheses

Compound	Competing phase	ΔG_f(eV)
Sc_2CaO_2C	Sc_2O_3 (Ia3), Sc, CaO, CaC_2	-1.48
	Sc, CaO, CO	-6.75
Ti_2CaO_2C	Ti_2O_3 ($R\bar{3}c$), Ti, CaO, CaC_2	-2.41
	TiO_2 ($I4_1/amd$), Ti, CaO, CaC_2	-2.90
	Ti, CaO, CO	-5.92
V_2CaO_2C	V_2O_3 ($R\bar{3}c$), V, CaO, CaC_2	-1.59
	V_2O_5 (Pmmn), V, CaO, CaC_2	-3.36
	V, CaO, CO	-3.44
Cr_2CaO_2C	Cr_2O_3 ($R\bar{3}c$), Cr, CaO, CaC_2	-0.13
	Cr, CaO, CO	-0.74
Mn_2CaO_2C	Mn_2O_3 (Ia3), Mn, CaO, CaC_2	-1.32
	Mn, CaO, CO	-0.23
Y_2CaO_2C	Y_2O_3 (Ia3), Y, CaO, CaC_2	-0.91
	Y, CaO, CO	-6.35
Zr_2CaO_2C	ZrO_2 ($I4_1/amd$), Zr, CaO, CaC_2	-2.28
	Zr, CaO, CO	-6.45
Nb_2CaO_2C	NbO_2 ($I4_1/a$), Nb, CaO, CaC_2	-1.91
	Nb_2O_5 (P2), Nb, CaO, CaC_2	-3.03
	Nb, CaO, CO	-4.06
Mo_2CaO_2C	MoO_2 ($P4_2/mnm$), Mo, CaO, CaC_2	-0.88
	Mo, CaO, CO	-1.85
La_2CaO_2C	La_2O_3 ($P\bar{3}m1$), La, CaO, CaC_2	-1.27
	La, CaO, CO	-4.13
Hf_2CaO_2C	HfO_2 ($P2_1/c$), Hf, CaO, CaC_2	-1.95
	Hf, CaO, CO	-6.39
Ta_2CaO_2C	Ta_2O_5 (C2/c), Ta, CaO, CaC_2	-2.31
	Ta, CaO, CO	-3.40

Table S3. The hole and electron effective masses (m_h and m_e) of MAOX semiconductors, where $\perp$ and $||$ represent the parallel and perpendicular directions. The average parallel effective masses of hole and electron are reported in Table 2 and listed here in bold

Compound	$m_h^{\|}$ (m_0)		$m_h^{\perp}$ (m_0)	$m_e^{\|}$ (m_0)		$m_e^{\perp}$ (m_0)
	Γ→M	Γ→K	Γ→A	M→Γ	M→K	M→L
Sc_2CaO_2C	2.05	1.97	2.28	0.69	0.24	0.49
	2.01			**0.47**		
	VBM→K	VBM→Γ	-	M→Γ	M→K	M→L
Cr_2CaO_2C	1.37	1.73		1.44	3.64	32.46
	1.55			**2.54**		
	Γ→M	Γ→K	Γ→A	M→Γ	M→K	M→L
Y_2CaO_2C	3.42	3.17	2.70	0.62	0.21	0.47
	3.30			**0.42**		
	VBM→K	VBM→Γ	-	A→H	A→L	A→Γ
Mo_2CaO_2C	0.44	0.87		0.34	0.35	0.80
	0.66			**0.35**		

	M→Γ	M→K	M→L	M→Γ	M→K	M→L
La_2CaO_2C	5.11	0.30	17.24	0.65	0.19	0.47
	2.71			**0.42**		

Table S4. The calculated shear moduli (G) and bulk moduli (K) of MAOX semiconductors according to the Voigt-Reuss-Hill approximation

Compound	G (GPa)	K (GPa)
Sc_2CaO_2C	102.4	149.4
Y_2CaO_2C	87.8	125.7
Cr_2CaO_2C	88.5	198.5
Mo_2CaO_2C	89.4	193.0
La_2CaO_2C	57.2	116.8

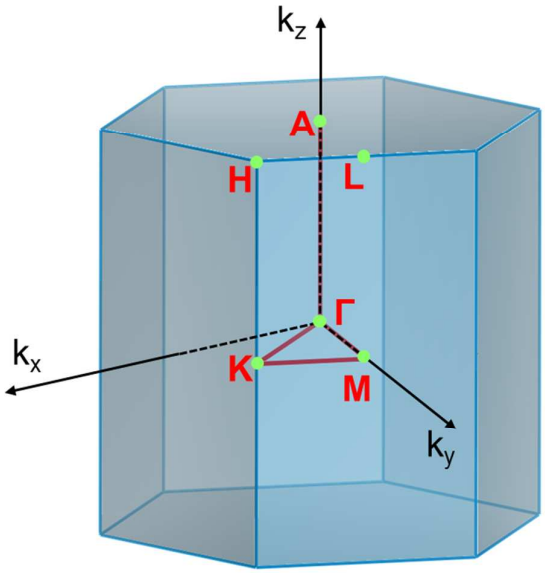

Figure S1. Brillouin zone of the P$\bar{3}$m1 space group. Coordinates of the high symmetry points used for the band structure: Γ = (0, 0, 0), M = (0, 1/2, 0), K = (1/3, 1/3, 0), A = (0, 0, 1/2), H = (1/3, 1/3, 1/2), L = (0, 1/2, 1/2).

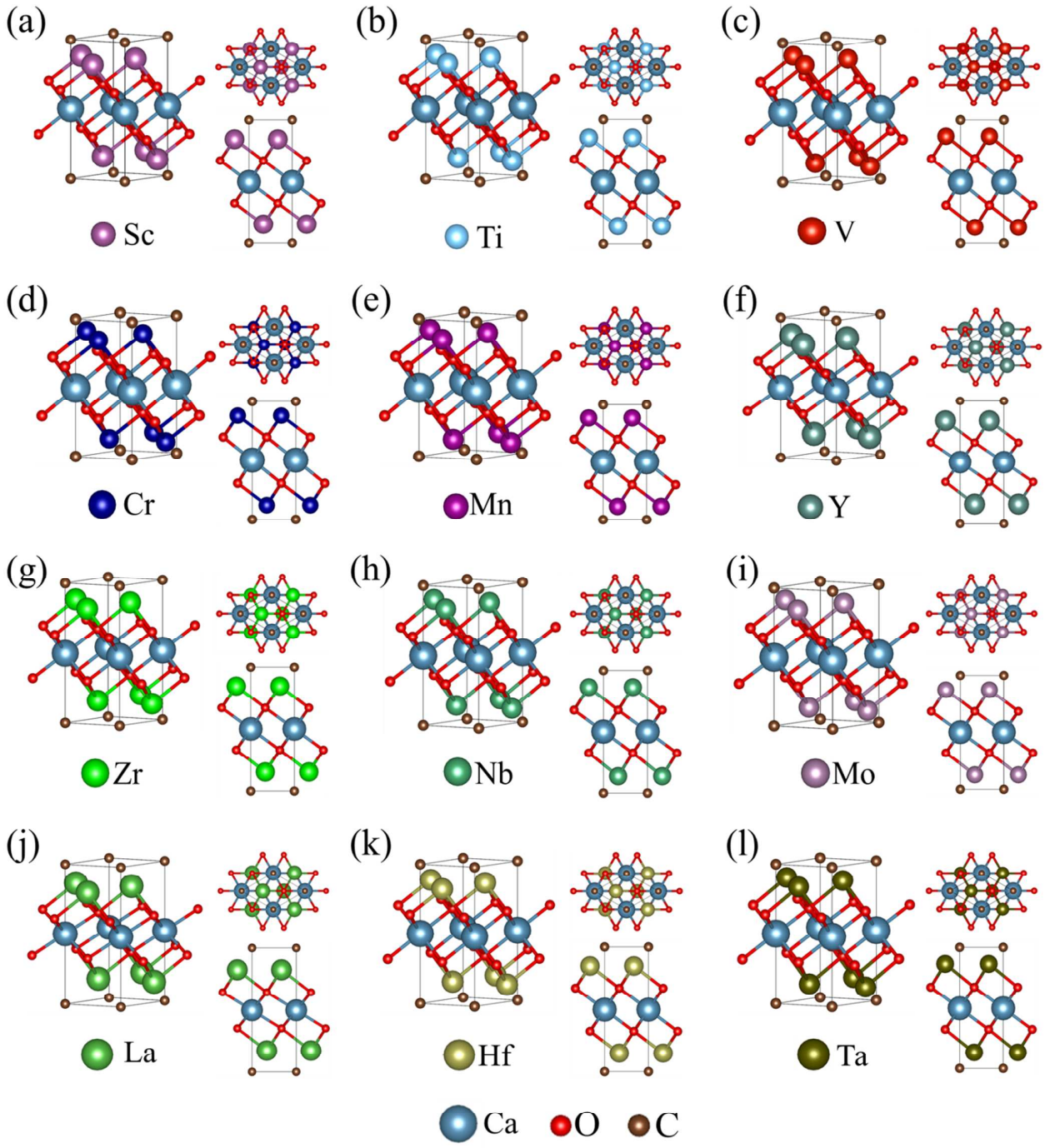

Figure S2. Relaxed structures of M_2CaO_2C unit cells: (a) Sc_2CaO_2C, (b) Ti_2CaO_2C, (c) V_2CaO_2C, (d) Cr_2CaO_2C, (e) Mn_2CaO_2C, (f) Y_2CaO_2C, (g) Zr_2CaO_2C, (h) Nb_2CaO_2C, (i) Mo_2CaO_2C, (j) La_2CaO_2C, (k) Hf_2CaO_2C and (l) Ta_2CaO_2C.

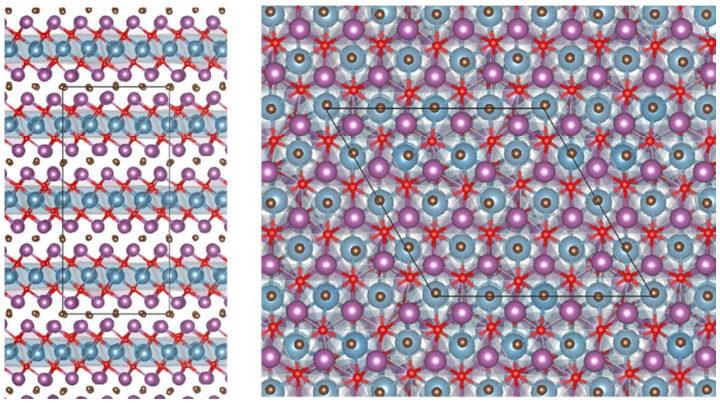

Figure S3. The AIMD simulation snapshots of Sc_2CaO_2C phase at 8 ps with temperature controlled at 1000 K in NVT ensemble. The shadow stands for the CaO_2 layers.

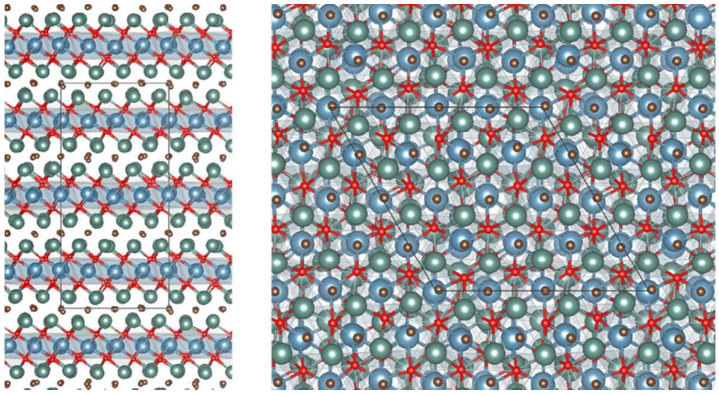

Figure S4. The AIMD simulation snapshots of Y_2CaO_2C phase at 8 ps with temperature controlled at 1000 K in NVT ensemble. The shadow stands for the CaO_2 layers.

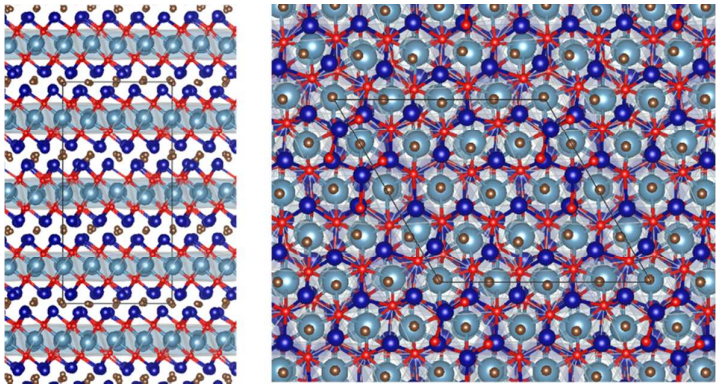

Figure S5. The AIMD simulation snapshots of the Cr_2CaO_2C phase at 8 ps with temperature controlled at 1000 K in NVT ensemble. The shadow stands for the CaO_2 layers.

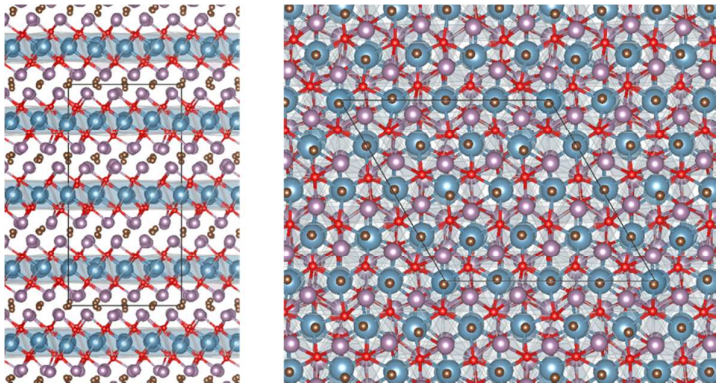

Figure S6. The AIMD simulation snapshots of Mo_2CaO_2C phase at 8 ps with temperature controlled at 1000 K in NVT ensemble. The shadow stands for the CaO_2 layers.

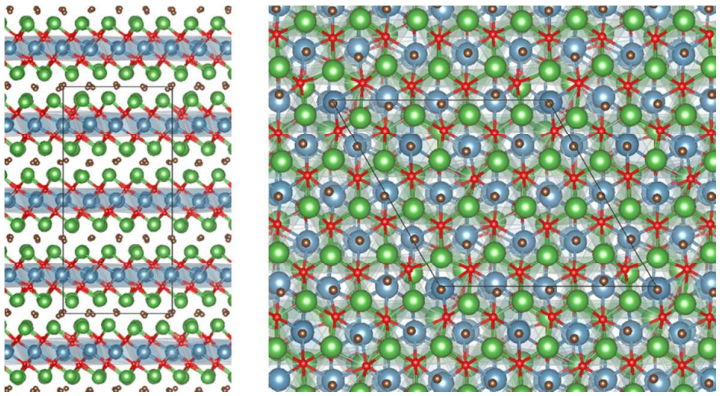

Figure S7. The AIMD simulation snapshots of La_2CaO_2C phase at 8 ps with temperature controlled at 1000 K in NVT ensemble. The shadow stands for the CaO_2 layers.

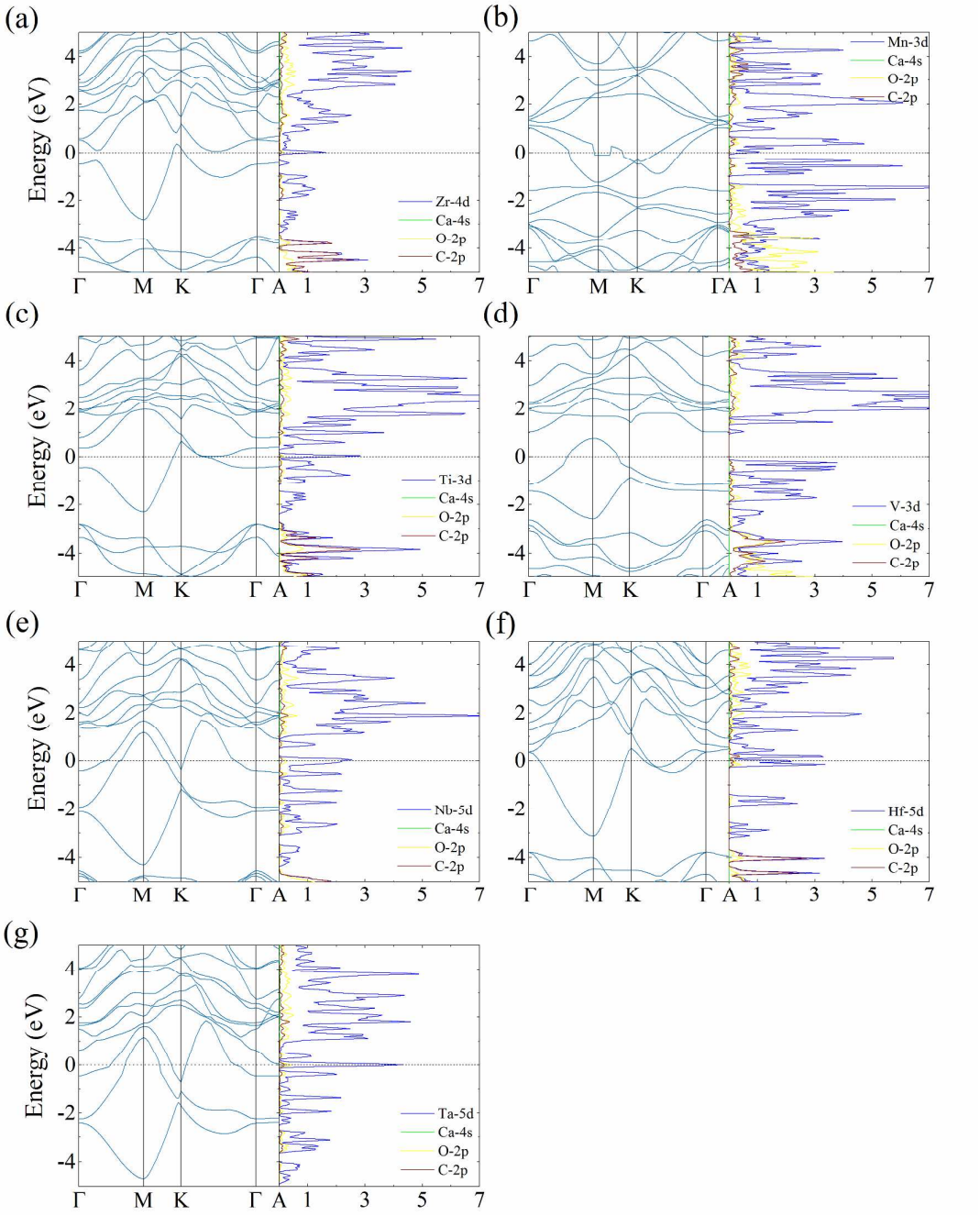

Figure S8. Band structures and projected DOS of the MAOX semimetal: (a) Zr_2CaO_2C; and the MAOX metals: (b) Mn_2CaO_2C, (c) Ti_2CaO_2C, (d) V_2CaO_2C, (e) Nb_2CaO_2C, (f) Hf_2CaO_2C and (g) Ta_2CaO_2C. The dash black line indicates the Fermi level.

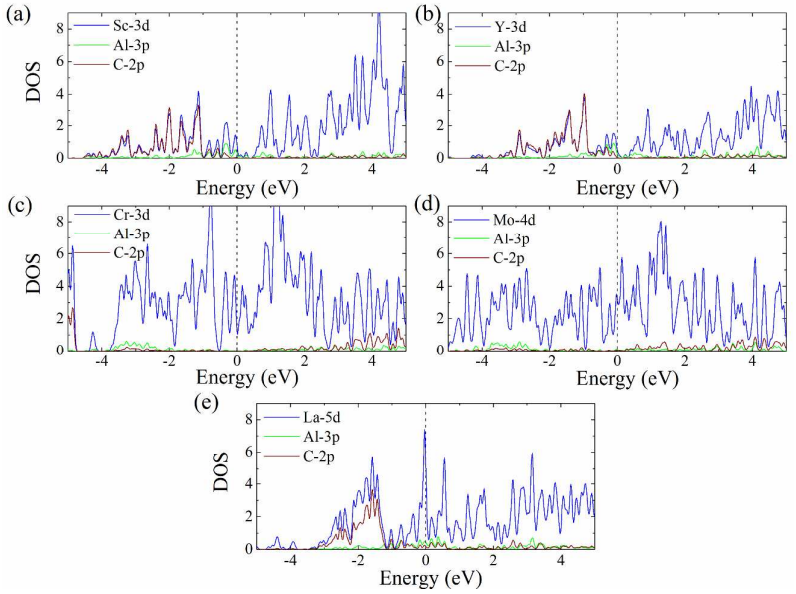

Figure S9. The projected DOS of the five 211 MAX phases: (a) Sc_2AlC, (b) Y_2AlC, (c) Cr_2AlC, (d) Mo_2AlC, and (e) La_2AlC. The dash black line indicates the Fermi level.

REFERENCES

(1) Shockley, W.; Queisser, H. J., Detailed Balance Limit of Efficiency of P-N Junction Solar Cells. *J. Appl. Phys.* **1961,** 32, 510-519.
(2) Yu, L. P.; Kokenyesi, R. S.; Keszler, D. A.; Zunger, A., Inverse Design of High Absorption Thin-Film Photovoltaic Materials. *Adv. Energy Mater.* **2013,** 3, 43-48.
(3) Yu, L. P.; Zunger, A., Identification of Potential Photovoltaic Absorbers Based on First-Principles Spectroscopic Screening of Materials. *Phys. Rev. Lett.* **2012,** 108, 068701.
(4) Blochl, P. E.; Jepsen, O.; Andersen, O. K., Improved Tetrahedron Method for Brillouin-Zone Integrations. *Phys. Rev. B* **1994,** 49, 16223-16233.
(5) Voigt, W., *Lehrbuch der Kristallphysik (mit Ausschluss der Kristalloptik)*. Vieweg+Teubner Verlag: 2014.
(6) Reuss, A., Berechnung der Fließgrenze von Mischkristallen auf Grund der Plastizitätsbedingung für Einkristalle. *Zeitschrift für Angewandte Mathematik und Mechanik* **1929,** 9, 49-58.
(7) Hill, R., The Elastic Behaviour of a Crystalline Aggregate. *P. Phys. Soc. Lond. A* **1952,** 65, 349-355.
(8) Khazaei, M.; Arai, M.; Sasaki, T.; Chung, C. Y.; Venkataramanan, N. S.; Estili, M.; Sakka, Y.; Kawazoe, Y., Novel Electronic and Magnetic Properties of Two-Dimensional Transition Metal Carbides and Nitrides. *Adv. Funct. Mater.* **2013,** 23, 2185-2192.
(9) Hong, L.; Klie, R. F.; Ogut, S., First-principles study of size- and edge-dependent properties of MXene nanoribbons. *Phys. Rev. B* **2016,** 93, 115412.
(10) Gandi, A. N.; Alshareef, H. N.; Schwingenschlogl, U., Thermoelectric Performance of the MXenes M_2CO_2 (M = Ti, Zr, or Hf). *Chem. Mater.* **2016,** 28, 1647-1652.
(11) Khazaei, M.; Arai, M.; Sasaki, T.; Estili, M.; Sakka, Y., Two-dimensional molybdenum carbides: potential thermoelectric materials of the MXene family. *Phys. Chem. Chem. Phys.* **2014,** 16, 7841-7849.